JOURNAL OF AIRCRAFT
Vol. 42, No. 5, September–October 2005

Near-Surface Topology of Unmanned Combat Air Vehicle Planform: Reynolds Number Dependence

M. Elkhoury,* M. M. Yavuz,† and D. Rockwell‡
Lehigh University, Bethlehem, Pennsylvania 18015

The Reynolds number dependence of the near-surface flow structure and topology on a representative unmanned combat air vehicle planform is characterized using a technique of high-image-density particle image velocimetry, to complement classical dye visualization. Patterns of streamline topology, including bifurcation lines, as well as contours of streamwise and transverse velocity, surface-normal vorticity, and Reynolds stress correlation, all immediately adjacent to the surface of the planform, provide quantitative indicators. At low angle of attack, these indicators show significant alterations with Reynolds number, in accord with large variations of patterns of vortex breakdown and vortex interaction visualized by dye and substantial alterations of flow patterns in the crossflow plane, including reattachment phenomena, which are interpreted with patterns of velocity, streamlines, and streamwise vorticity. On the other hand, at moderate angle of attack, the near-surface quantitative indicators show much less sensitivity to Reynolds number, which is in line with weak variations of the onset of vortex breakdown with changes in Reynolds number.

I. Introduction

ACTUAL aerodynamic planforms involve complex and abrupt changes in leading-edge sweep angle. As a consequence, two or more vortex systems are typically generated on each half of the planform. The consequent interaction between vortices has been pursued in several investigations. For the case of a double-delta planform, Hebbar et al.[1] assess the consequence of variation of Reynolds number on the vortex patterns, which were visualized with dye injection. This visualization was complemented with laser Doppler velocimetry, to define features of the vortex structure and interaction further. A principal finding is that the degree of interaction between the vortex emanating from the apex of the fuselage and the vortex from wing root was a strong function of Reynolds number. Whereas significant interaction occurred at lower values of Reynolds number, these vortices developed in a relatively decoupled fashion at higher Reynolds number. This change in the flow pattern at high Reynolds number was accompanied by an enhanced deflection of the wing root vortex in the outboard direction. Verhaagen[2] gives a comprehensive assessment of the major features of the vortex system, principally the manner in which the vortices develop and interact, taking into account the influence of Reynolds number. Among the characterizations in his summary is surface oil film visualization, which provides an indication of the time-averaged patterns of surface shear stress in relation to Reynolds number. Visser and Washburn[3] and Verhaagen et al.[4] consider the effects of relatively high Reynolds number, in the range from 0.5 to 2.5×10^6 and, in most cases, account for changes of angle of attack. Issues related to transition of the boundary layer, in relation to the strength of the primary vortex, are assessed by Visser and Washburn.[3] Furthermore, characterizations of the surface pressure coefficient, and topology of the surface flow patterns, are addressed as a function of Reynolds number by Verhaagen et al.[4]

Whereas the foregoing investigations have focused primarily on planforms having relatively large values of sweep angle, unmanned combat air vehicle (UCAV) planforms are characterized by relatively low values of sweep angle of the leading portions of the fuselage and wing extension. For the case of a simple delta wing of low sweep angle, Yaniktepe and Rockwell[5] show that the flow structure in the crossflow plane involves an elongated layer of vorticity along the edge of a relatively narrow zone of separated flow; this layer tended to attach to the wing surface. This type of flow structure in the crossflow plane is not seen on wings of relatively high sweep angle, which exhibit a single, large-scale primary vortex, fed by the separated vorticity layer from the leading edge of the wing. Furthermore, for wings of moderate to low sweep angle of the order of $\Lambda = 50$ deg, a single, large-scale vortex occurs at sufficiently high Reynolds number, as shown by Gordnier and Visbal.[6] Additional aspects of the flow structure on a delta wing of relatively low sweep angle are addressed by Ol and Gharib,[7,8] Yaniktepe and Rockwell,[5] and Yavuz et al.[9] For the case of a UCAV planform, Elkhoury and Rockwell[10] provide dye visualization images over a range of angles of attack and Reynolds numbers, accounting for the coexistence of vortices emanating from the apex and the junction of the wing, as well as their potential interaction, and the onset of vortex breakdown.

Gordnier and Visbal[6] used a high-order compact difference scheme to simulate the flow on a delta wing planform of sweep angle $\Lambda = 50$ deg. At low Reynolds number, a thick separated shear layer with strong viscous interaction is seen, whereas with increasing the Reynolds number, the viscous effect is reduced and a dual vortex structure develops. The vortex structure changes from an elongated shear layer at low angle of attack to a circularlike vortical structure at higher angle of attack. The flow structure on the same planform was addressed experimentally by Taylor et al.[11] They reported that the vortex breakdown and the core trajectory depend on both the Reynolds number and the angle of attack, which is in agreement with the present findings. The shear layer forms very close to the wing surface at low values of angle of attack and lifts from the surface and takes a nearly circular form with an increase in angle of attack. The existence of a dual vortex structure was also reported. Their investigation employed dye visualization along with a digital particle image velocimetry measurement technique.

At low Reynolds number, the flow structure over UCAVs, unmanned air vehicles, and microair vehicles is highly sensitive to variations in Reynolds number. This in turn, is an important issue

Received 2 April 2004; revision received 16 June 2004; accepted for publication 21 June 2004.

*Research Assistant, Department of Mechanical Engineering and Mechanics, 356 Packard Laboratory, 19 Memorial Drive West; currently Assistant Professor, Department of Mechanical Engineering, American University Lebanon. Member AIAA.

†Research Assistant, Department of Mechanical Engineering and Mechanics, 356 Packard Laboratory, 19 Memorial Drive West.

‡Paul B. Reinhold Professor, Department of Mechanical Engineering and Mechanics, 356 Packard Laboratory, 19 Memorial Drive West; dor0@lehigh.edu. Member AIAA.

because the operation range of such vehicles falls within a low Reynolds number range and could include vortex–vortex interaction and vortex–boundary-layer interaction. Gursul et al.[12] and Gursul[13] provide insight into the effects of Reynolds number on the vortical flows over these vehicles.

All of the foregoing aspects of the flow structure on wings and planforms having low to moderate values of sweep angle can potentially be interpreted with the aid of topological concepts based on critical point theory, which has been used in variety of aerodynamic applications. Experimental investigations have visualized the surface shear stress patterns via a thin oil film or its equivalent. Perry and Fairly[14] and Tobak and Peake[15] assessed interpretation of complex surface patterns via critical point theory. Lighthill[16] and Squire[17] addressed theoretically the relation between streamlines and surface shear stress lines whereas Hunt et al.[18] specified criteria for similarity of the patterns of critical points of the surface shear stress and the surface velocity field and, thereby, streamlines. When these criteria are satisfied, the shear stress lines may also be interpreted as surface streamlines. The aim of the present investigation, however, is not to represent the shear stress lines via the surface streamlines, nor to interpret the full details of the surface topology based on the critical point theory. Rather, it is intended to characterize the effect of Reynolds number on the overall features of the separation and reattachment processes via the near-surface bifurcation lines.

Characterization of the effects of Reynolds number on the flow past actual aerodynamic planforms has primarily focused on qualitative visualization using dye marker techniques, with some complementary quantitative measurements. Although such qualitative indicators are valuable in characterizing the onset of vortex breakdown, as well as vortex–vortex interaction, it is desirable to employ a quantitative, wholefield method to obtain quantitative representations of the surface flow patterns, accounting for both steady (time-averaged) and unsteady features of the flow immediately adjacent to the surface. Such representations can lead to the following interpretations of the flow structure.

Streamline Topology

Patterns of mean (time-averaged), near-surface streamlines are expected to exhibit basic topological features, such as bifurcation lines, which may be associated with separation and reattachment phenomena, as well as other physical characteristics. The existence and alteration of such bifurcation lines as a function of Reynolds number have not been addressed.

Contours of Streamwise and Transverse Velocity Components

Contour patterns of the principal velocity components immediately adjacent to the surface can provide an indication of regions of near-surface acceleration, deceleration, and flow reversal. The manner in which these contour patterns change with Reynolds number has remained unexplored.

Patterns of Surface-Normal Vorticity

Vorticity from the windward side of the wing, evident along the leading edges, as well as vorticity associated with the development of ordered vortices along the wing surface, provides a quantitative portrayal of the flow structure that has not been addressed as a function of Reynolds number. On the surface of the wing, the degree of concentration of contours of surface-normal vorticity, as well as the number and sign of these concentrations, can provide insightful representations of the footprint of the complex processes of vortex breakdown and vortex interaction, especially at the location of the wing junction and in the vicinity of the trailing edge.

Patterns of Reynolds Stress Correlation

The occurrence of unsteadiness along the wing surface, including the onset of vortex breakdown, is reflected in the magnitude of, and phase angle between, velocity fluctuations. The Reynolds stress correlation can provide an indicator of the increasingly predominant role of vortex unsteadiness/breakdown with increasing Reynolds number.

Instantaneous Representations of the Flow Patterns

The foregoing characterizations of the flow structure involve time-averaged patterns. Examination of representative instantaneous patterns of, for example, streamline topology and surface-normal vorticity, can provide indicators of the degree of deviation of the instantaneous states from the corresponding time-averaged state.

To date, the foregoing types of quantitative indicators have not been addressed for a UCAV configuration over a range of Reynolds number. The aim of the present investigation is to address these features using a technique of high-image-density particle image velocimetry, in conjunction with appropriate postprocessing techniques.

II. Experimental System and Techniques

Experiments were conducted in a low-turbulence water channel, with a test section of cross section 927×610 mm and length 4928 mm. The turbulent intensity at the entrance of the test section was less than 0.2%. The wing used in this investigation was a model of a Boeing X-45A UCAV with a flat planform of thickness 3 mm. All leading edges were beveled on the windward side at an angle of 30 deg. The UCAV model had a chord length of 188 mm from nose to tail and a wing span of 251 mm. The apex of the fuselage and the wing root had sweep angles of 45 and 40 deg, respectively. The Reynolds numbers used in this investigation, based on the chord length C of the planform, were 1×10^4, 2×10^4, and 4×10^4. The angles of attack were $\alpha = 7$ and 13 deg.

A high-image-density particle image velocimetry (PIV) technique was employed to quantitatively determine the flow structure. Schematics that represent both the near-surface and the crossflow imaging are given in Fig. 1. Illumination was provided by a dual-pulse Yag laser system, having a maximum output of 90 mJ. To characterize the near-surface flow patterns, the collinear beam from this dual laser system was transmitted through a system of cylindrical and spherical lenses attached to the laser head. The flow was seeded with 12-μm metallic-coated, hollow plastic spheres, which were essentially neutrally buoyant. Patterns of particle images were recorded on a high-resolution camera, having 1024×1024 pixels, with an effective framing rate of 15 cycles/s. For imaging of the near-surface patterns, the camera was located beneath the channel, and its axis was perpendicular to the planform surface, as indicated by the view arrow in Fig. 1. The distance from the sensor of the camera to the surface of the planform was 119 cm. The center of the laser sheet was at a distance of $z = 1$ mm from the surface of the planform; therefore, $z/C = 0.0053$.

For imaging in the crossflow plane, the laser–camera arrangement was fundamentally different. The collinear beam from the laser was deflected 90 deg through a prism located underneath the channel, then passed through the system of cylindrical and spherical lenses. Images in the crossflow plane were deflected exterior to the test section via a small mirror and recorded by the high-resolution camera, whose axis was perpendicular to the vertical wall of the test section. The distance from the imaging crossflow plane to the mirror was 76 cm, and that from the mirror to the sensor of the camera was 74 cm. Because of laser reflection from the surface of the planform during imaging in the crossflow plane, it was not possible to determine accurately the patterns of velocity in the region close to the planform surface, as indicated by the blank regions between the edge of the field of view and the surface. As a result, it is not possible to identify precisely the locations of possible separation from, and reattachment to, the surface in the crossflow plane.

During evaluation of the velocity field, two sizes of interrogation windows were employed: 32×32 pixels and 16×16 pixels. For the near-surface patterns, the effective resolution, that is, grid size, was $\Delta = 4.67$ mm, corresponding to $\Delta/C = 0.025$ for the large interrogation window (32×32) and $\Delta = 2.34$ mm, corresponding to $\Delta/C = 0.012$ for the small interrogation window (16×16). For the large and small interrogation windows of the crossflow plane,

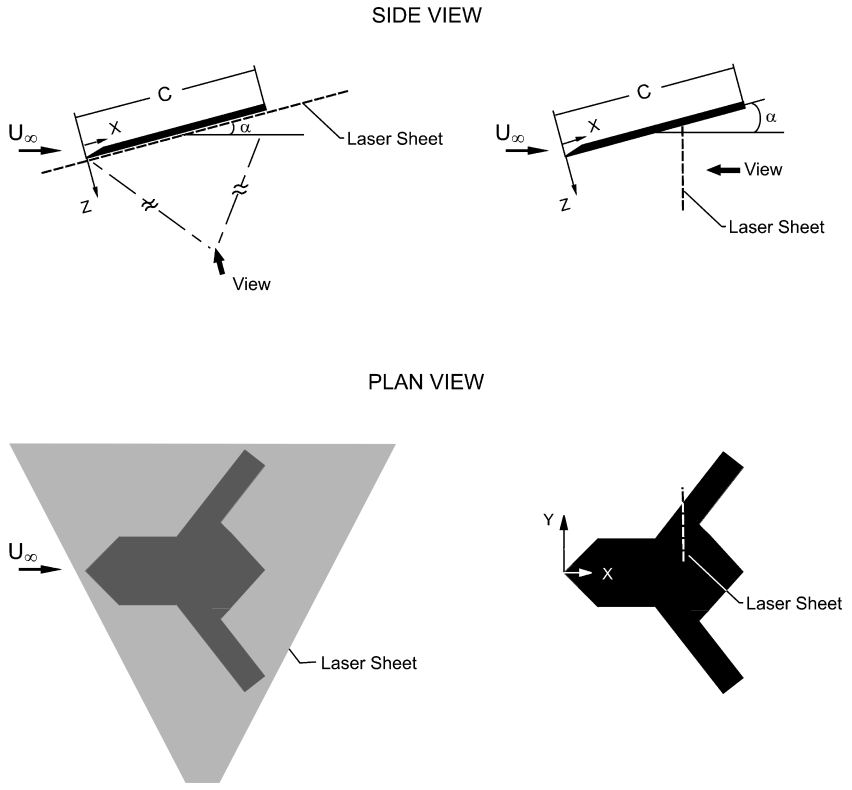

Fig. 1 Overview of UCAV planform, laser sheet locations, and orientations for near-surface and crossflow imaging.

$\Delta = 1.43$ and $\Delta = 0.72$ mm, corresponding to $\Delta/C = 0.0076$ and $\Delta/C = 0.00384$, respectively. In all cases, the effective overlap was 50%, to satisfy the Nyquist criterion. The smaller interrogation window was used only for imaging in the crossflow plane and for verification of imaging with the large window in the near-surface plane.

The blockage in the water channel due to the presence of the planform is defined as the ratio of the projected area (perpendicular to the flow) of the planform at the highest angle of attack, 13 deg, to the channel cross-sectional area; this ratio is 0.0076. The principal uncertainties of the experimental system are as follows. The uncertainty of the angle of attack of the planform was 0.2 deg. The overall accuracy of the PIV method is estimated to yield a maximum uncertainty of local velocity of 1.5%. Furthermore, because of the relatively large distance from the laser sheet to the sensor of the camera, normalized by the half-width of the field of view in the plane of the laser sheet, the paraxial recording criterion was well satisfied, and therefore, contributions of out-of-plane motion to the distortions of the two-dimensional velocity field in the plane of the laser sheet are less than 1%.

III. Near-Surface Patterns at Low Angle of Attack

Patterns of Dye Visualization and Near-Surface Time-Averaged Streamline Topology

Figures 2–6 show various representations of the flow patterns at a relatively low angle of attack $\alpha = 7$ deg over the range of Reynolds number extending from $Re = 1 \times 10^4$ to 4×10^4. Figures 2–6 provide cross comparisons with qualitative dye visualization, instantaneous and averaged streamline topology, and surface-normal vorticity, as well as averaged patterns of velocity contours and Reynolds stress correlations.

Figure 2a provides classical, qualitative dye visualization of the vortices emanating from the apex of the fuselage, as well as from the wing junction, and their degree of interaction. Figure 2a shows excerpts from a large number of dye visualizations over a range of Reynolds number, described by Elkhoury and Rockwell.[10] It is evident from Fig. 2a that, as the Reynolds number increases, the onset of vortex breakdown of the vortices formed from the apex moves upstream. Simultaneously, the vortex formed from the wing junction is deflected in the outboard direction, and the degree of interaction decreases between the vortices originating from the apex and the wing junction.

Corresponding patterns of time-averaged streamline topology $\langle\Psi\rangle$ are given in Fig. 2b. Consider, first, the pattern at $Re = 1 \times 10^4$. Over the right half of the wing, a positive bifurcation line, that is, a line along which individual streamlines branch out, is designated as BL^+. This line occurs well inboard of the leading edge of the wing. In addition, a negative bifurcation line BL^- occurs immediately inboard of the leading edge.

As the value of Reynolds number increases to $Re = 2 \times 10^4$ and 4×10^4, the middle and bottom images of $\langle\Psi\rangle$ in Fig. 2b show transverse movement of both the positive and negative bifurcation lines BL^+ and BL^- in the outboard direction. For reference, ○ represents the location of the notch of the trailing edge. At $Re = 2 \times 10^4$, BL^+ intersects the location of the notch ○, and at $Re = 4 \times 10^4$, it is displaced a significant distance to the right of ○. Simultaneously, the negative bifurcation line BL^- moves closer to the leading edge for successive increases of Reynolds number Re to 2×10^4 and 4×10^4.

Additional observations of the alteration of the patterns of $\langle\Psi\rangle$ in Fig. 2b include the distance between the positive bifurcation lines BL^+ on either side of the plane of symmetry of the wing. This distance, which is most clearly evident at a streamwise location corresponding to the apex of the planform, increases with increasing values of Reynolds number Re. A further, subtle point is the occurrence of secondary bifurcation lines, designated as $(BL^+)_s$ at $Re = 4 \times 10^4$. Generally speaking, there is lack of symmetry of the patterns. As will be addressed subsequently, very subtle changes in the contours of constant streamwise and transverse velocity, that is, mild asymmetries with respect to the plane of asymmetry of the wing, are associated with these deviations from symmetry of the $\langle\Psi\rangle$ patterns at $Re = 4 \times 10^4$.

A further point concerns the existence of a negative bifurcation line BL^- between the two positive bifurcation lines designated as BL^+ and $(BL^+)_s$. This negative bifurcation line BL^- is clearly

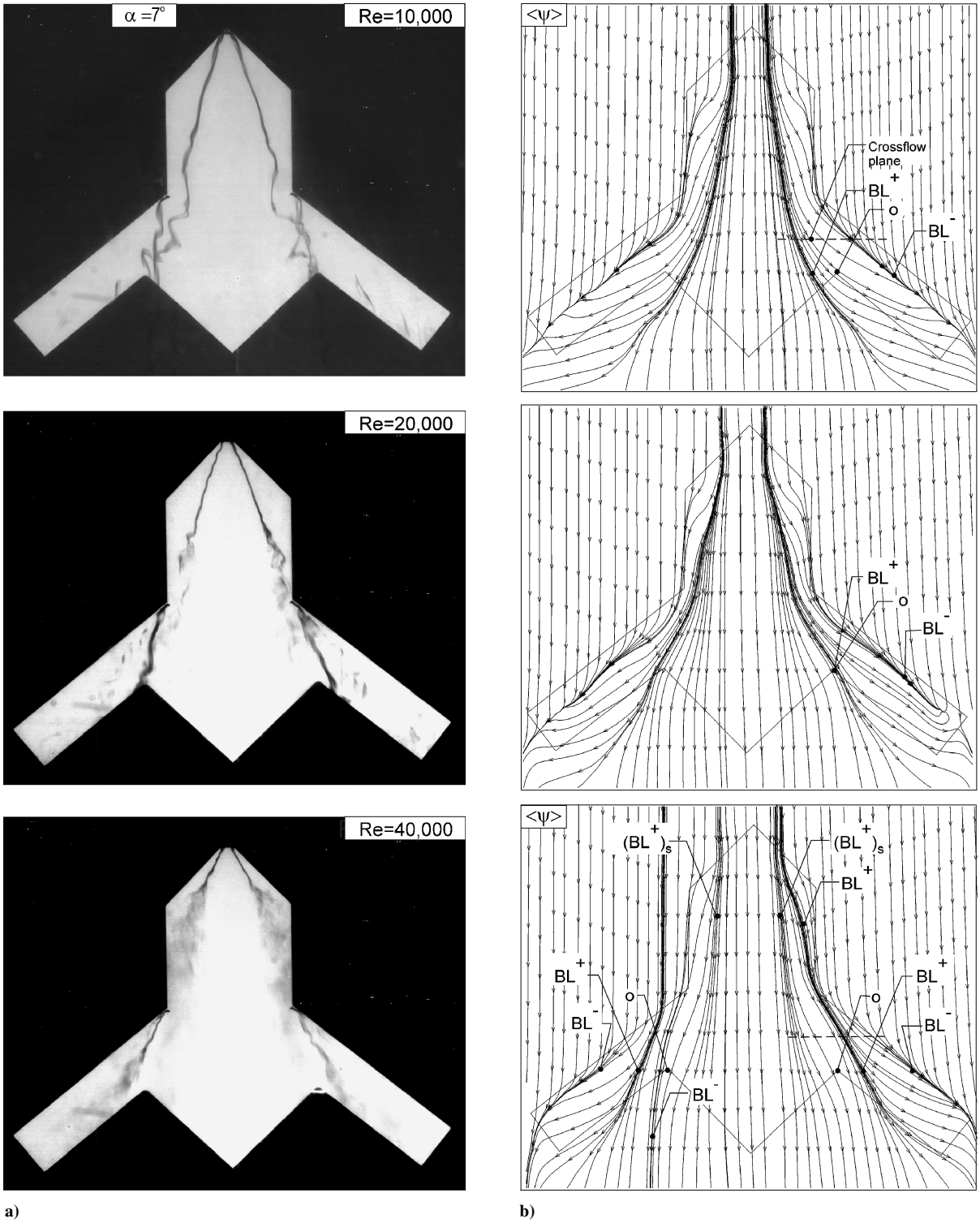

Fig. 2 Comparison of patterns of dye visualization with near-surface patterns of streamline topology $\langle \Psi \rangle$.

evident at the designated location on the left side of the planform, but is not evident on the right side of the planform at $Re = 4 \times 10^4$ in Fig. 2b. A zoomed-in view of this region, employing a high resolution interrogation of the original data (not shown here) does indicate formation of a weak, negative bifurcation line BL^-.

Direct comparison of the patterns of dye, which indicate the onset of vortex breakdown, with the form of the positive bifurcation line $(BL^+)_s$, shows the following interrelationship as a function of Reynolds number. At relatively low $Re = 1 \times 10^4$, where the onset of vortex breakdown occurs relatively far downstream, and in a gradual, spiral-like form, the corresponding BL^+ retains a well-defined form along the entire streamwise extent of the planform and even into the near-wake region. That is, very closely spaced streamlines persist along this entire extent. At $Re = 2 \times 10^4$, vortex breakdown moves farther upstream, and the wing root vortex is deflected outward; in this case, the onset of rapid streamline divergence of the BL^+ is evident at approximately the location of onset of vortex breakdown. Finally, at $Re = 4 \times 10^4$, vortex breakdown moves even closer to the apex of the fuselage, and one sees, at least on the right side of the planform, formation of the two positive bifurcation lines $(BL^+)_s$ and BL^+ at approximately the onset of vortex breakdown.

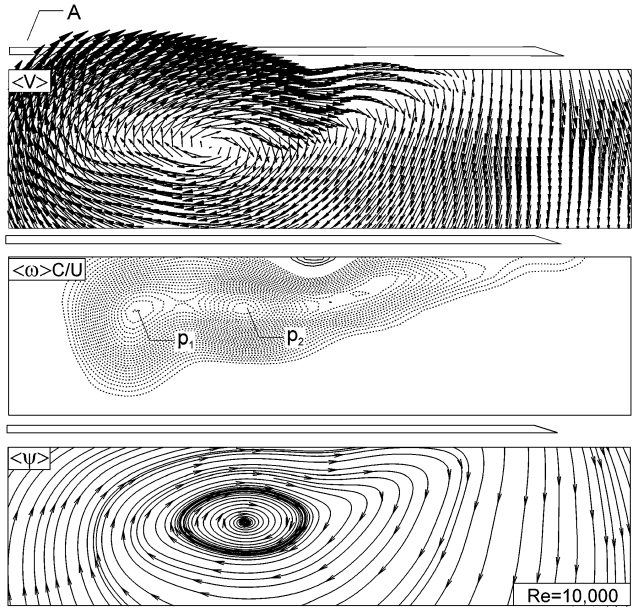

a)

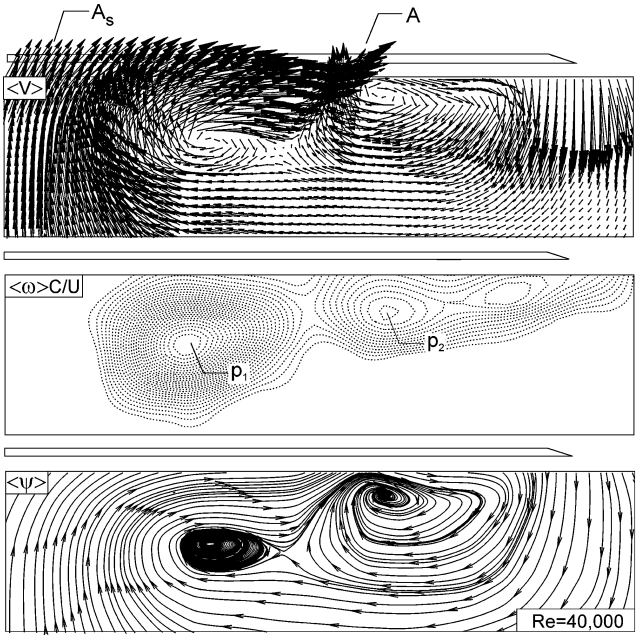

b)

Fig. 3 Patterns of time-averaged velocity vectors $\langle V \rangle$, vorticity $\langle \omega \rangle C/U$, and streamlines $\langle \Psi \rangle$ in the crossflow plane at streamwise location in Fig. 2b.

Patterns of Velocity and Vorticity in Crossflow Plane

Figure 3 shows zoomed-in images of the flow structure in the crossflow plane, which emphasize the region adjacent to the surface, with the intent of clarifying the physical interpretation of the bifurcation lines BL^+ and BL^- given in Fig. 2b. The streamwise distance corresponds to $x/C = 0.644$. This location, as well as the spanwise extent of the field of view, is indicated by the dashed line in the plan view images at $Re = 1 \times 10^4$ and 4×10^4 in Fig. 2b. As indicated therein, this streamwise location corresponds to the region immediately downstream of the wing junction, and therefore, the consequences of vortices emanating from both the apex and the junction are accounted for. Figure 3a shows patterns of time-averaged velocity $\langle V \rangle$, normalized vorticity $\langle \omega \rangle C/U$, and streamlines $\langle \Psi \rangle$ at the lowest Reynolds number $Re = 1 \times 10^4$, whereas Fig. 3b corresponds to $Re = 4 \times 10^4$. For vorticity contours, minimum and incremental values of $\langle \omega \rangle C/U$ are 3.0 and 1.0.

Compare, first, the patterns of vorticity $\langle \omega \rangle C/U$ in the crossflow plane at $Re = 1 \times 10^4$ and 4×10^4 in Fig. 3. At the lower value of Reynolds number, two closely based concentrations, p_1 and p_2, are evident. They are apparently due to the time-averaged consequence of the intertwining dye markers shown in the visualization image at the top of Fig. 2a. On the other hand, at $Re = 4 \times 10^4$, these vorticity maxima p_1 and p_2 are substantially separated, corresponding to the non-intertwined nature of the vortices emanating from the wing junction and from the fuselage apex, indicated in the visualization at the bottom Fig. 2a. Furthermore, the corresponding patterns of velocity vectors $\langle V \rangle$ and streamlines $\langle \Psi \rangle$ at $Re = 1 \times 10^4$ indicate a single, large-scale swirl, due to the close proximity of the vorticity maxima p_1 and p_2, whereas at $Re = 4 \times 10^4$, two distinct swirl regions are evident in the patterns of $\langle V \rangle$ and streamlines $\langle \Psi \rangle$.

At $Re = 1 \times 10^4$, the patterns of velocity vectors $\langle V \rangle$ and streamlines $\langle \Psi \rangle$ in Fig. 3a show an elongated region of separated flow that tends to attach to the surface of the wing at location A, which corresponds, in the top of Fig. 2b, to the intersection of the line BL^+ with the dashed line that represent the field of view of the crossflow plane. That is, in this crossflow plane of Fig. 3a, shear layer reattachment to the surface of the wing tends to occur, in contrast to what one expects on a wing of relatively large sweep angle, that is, formation of a single, large-scale vortex adjacent to the surface of the wing.

At $Re = 4 \times 10^4$ in Fig. 3b, the patterns of $\langle V \rangle$ and $\langle \Psi \rangle$ indicate that the separated shear layer tends to reattach to the wing surface at a location much closer to the leading edge. This position is again designated as A, which, in the pattern of streamline $\langle \Psi \rangle$ topology of Fig. 2b, corresponds to the intersection of the bifurcation line BL^+ with the dashed line. The location A_s represents a vaguely defined location of attachment, and in the $\langle \Psi \rangle$ image of Fig. 2b, it corresponds to the intersection of the secondary bifurcation line $(BL^+)_s$ with the dashed line. Note that, at this location, $(BL^+)_s$ is ill defined, that is, the streamlines have substantially diverged from the very closely spaced streamlines evident farther upstream; as a consequence, it is difficult to connect directly the so-called location of $(BL^+)_s$ at this streamwise position to the apparent location of attachment A_s in the patterns of $\langle V \rangle$ and $\langle \Psi \rangle$ of Fig. 3b.

Patterns of Near-Surface Time-Averaged Transverse and Streamwise Velocity Components

The aforementioned changes in streamline topology with Reynolds number Re are related to corresponding variations of the contours of constant transverse $\langle v \rangle / U$ and streamwise $\langle u \rangle / U$ velocity components. First consider the patterns of transverse $\langle v \rangle / U$ given in Fig. 4a. Minimum and incremental values of $\langle v \rangle / U$ are 0.05 and 0.025. At $Re = 1 \times 10^4$, the closed contour b, which represents a local maximum, is located immediately downstream of the wing junction, whereas the maximum d is located in the near wake of the wing. At $Re = 2 \times 10^4$, a new maximum a appears on the fuselage. At a still higher value of $Re = 4 \times 10^4$, the pattern of $\langle v \rangle / U$ becomes even more complex. Maximum a has moved significantly closer to the apex of the fuselage, maximum b has degenerated into two maxima b_1 and b_2, and an additional maximum c appears. In the meantime, maximum d has continued to move in the upstream direction and is now coincident with the trailing edge of the wing. The evolution of these patterns of $\langle v \rangle / U$ with increasing Reynolds number allows further interpretation of the patterns of time-averaged streamline $\langle \Psi \rangle$ topology addressed in Fig. 2b. Close examination of the positive bifurcation line BL^+ shows that its locus not only moves in the outboard direction, but it is also distorted in such a manner as to effect an increasingly prevalent transverse component $\langle v \rangle / U$ with increasing values of Reynolds number Re. In fact, upstream migration of the extremum a in the contour plots of $\langle v \rangle / U$ in Fig. 4a occurs with increasing values of Reynolds number Re. This distortion tends to occur closer to the leading edge for increasing Reynolds number Re.

Corresponding patterns of streamwise velocity $\langle u \rangle / U$ are indicated in Fig. 4b. Minimum and incremental values of $\langle u \rangle / U$ are 0 and 0.04 respectively. A cluster of contours whose minimum is designated by f is essentially centered on the plane of symmetry of the

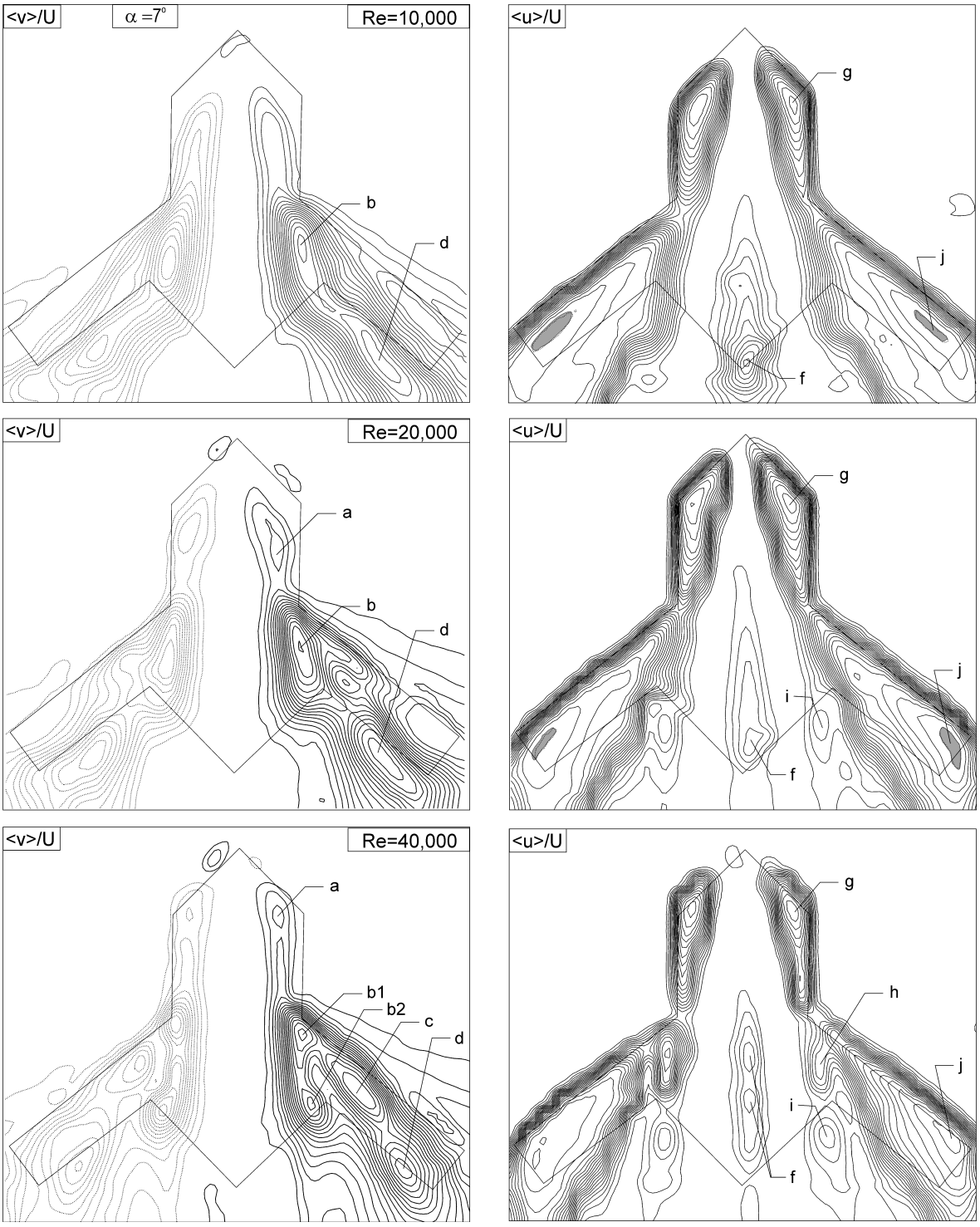

Fig. 4 Comparison of patterns of transverse $\langle v \rangle / U$ and streamwise $\langle u \rangle / U$ velocity contours: a) patterns of $\langle v \rangle / U$, extrema a through d represent local maxima and b) pattern of $\langle u \rangle / U$, extrema f through j represent local minima.

wing at all values of Reynolds number Re. The minimum f moves upstream from the trailing edge with increasing Reynolds number Re. In essence, the leading-half (up to the minimum value) of each set of these f contours represents a region of decelerating flow. On the other hand, the trailing-half of each cluster represents a region of accelerating flow. Furthermore, in the apex region, immediately inboard of the leading edge of the wing, local minima, that is, closed contours, of $\langle u \rangle / U$ are evident. The positive minimum designated as g is relatively close to the apex of the fuselage. Furthermore, a minimum j occurs near the wing tip. The sign of the shaded contour j is negative, and so a local region of reverse flow exists along that part of the wing surface. As the Reynolds number is increased from $Re = 1 \times 10^4$ to 2×10^4, then 4×10^4, the location of g is not significantly altered. On the other hand, the location of the localized region j of negative $\langle u \rangle / U$ moves in the outboard direction toward the tip of the wing at $Re = 2 \times 10^4$, then, at $Re = 4 \times 10^4$, the negative minimum j vanishes in favor of a positive minimum. In addition to this alteration of the region j at $Re = 2 \times 10^4$, additional closed contours of $\langle u \rangle / U$ appear; they are designated as h and i and represent positive minima. When the Reynolds number is increased to $Re = 4 \times 10^4$, the location of i is relatively unaffected.

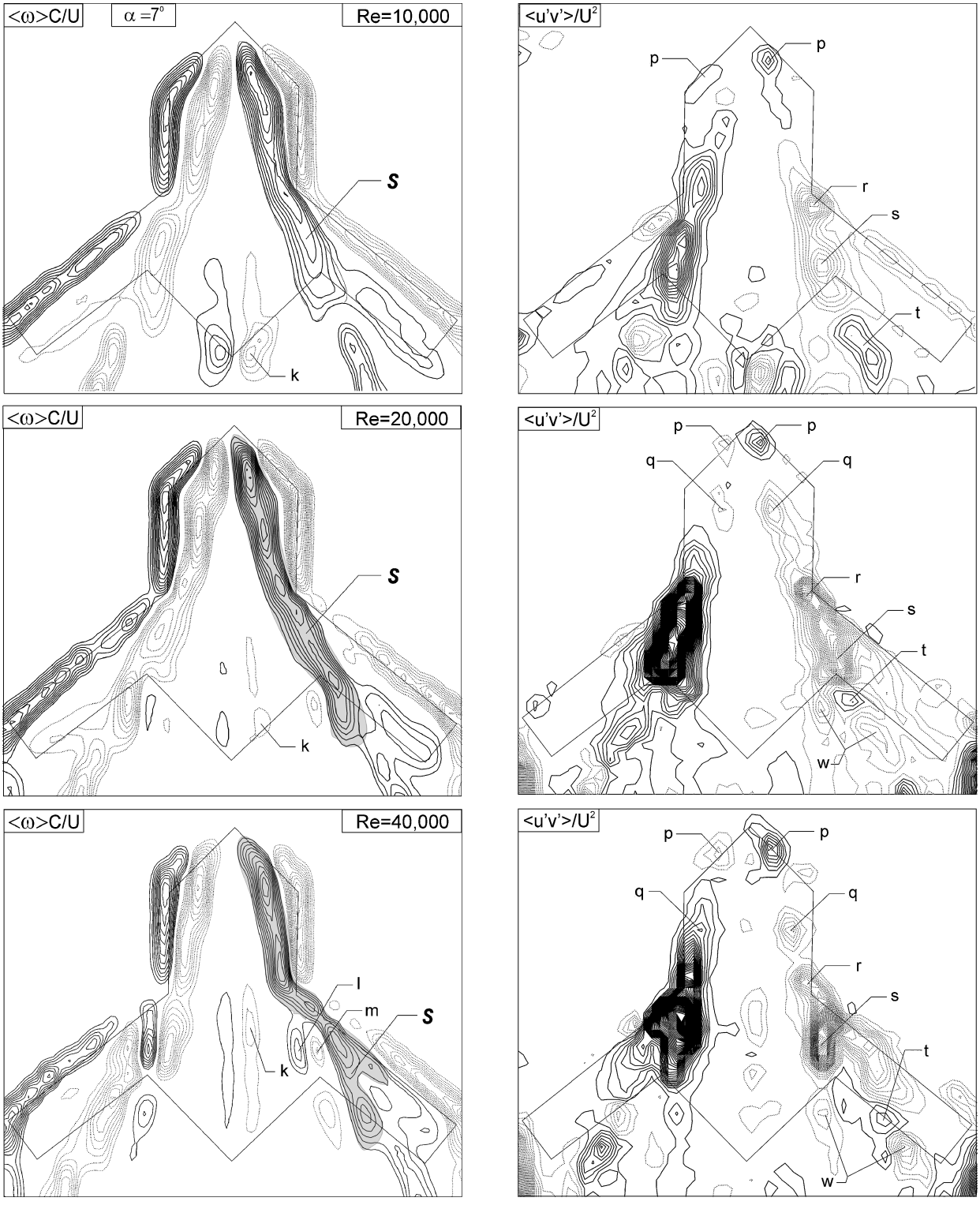

a) b)

Fig. 5 Comparison of patterns of normalized time-averaged vorticity $\langle\omega\rangle C/U$ and Reynolds stress correlation $\langle u'v'\rangle/U^2$.

Patterns of Surface-Normal Vorticity and Near-Surface Reynolds Stress Correlations

Patterns of time-averaged, dimensionless surface-normal vorticity $\langle\omega\rangle C/U$ are given in Fig. 5a. For vorticity contours, minimum and incremental absolute values of $\langle\omega\rangle C/U$ are 2.0 and 1.0. Near the plane of symmetry of the wing, at a location adjacent to the trailing edge, a set of clusters k appears. These clusters indicate the occurrence of a three-dimensional distortion near the trailing edge. At higher values of $Re = 2 \times 10^4$ and 4×10^4, the peak values of these vorticity clusters decrease, and they move upstream. The elongated (undesignated) patterns of vorticity contours along the leading edge of the wing are associated with separation of the three-dimensional boundary layer from the windward surface of the wing. Inboard of the leading edges, well-defined elongated clusters appear. The highest regions of vorticity on the starboard side of the wing are shaded in light gray, and the entire shaded region is designated ***S***. Comparison with the dye markers of Fig. 2 at $Re = 1 \times 10^4$ indicates that this shaded region is essentially a near-surface footprint of the

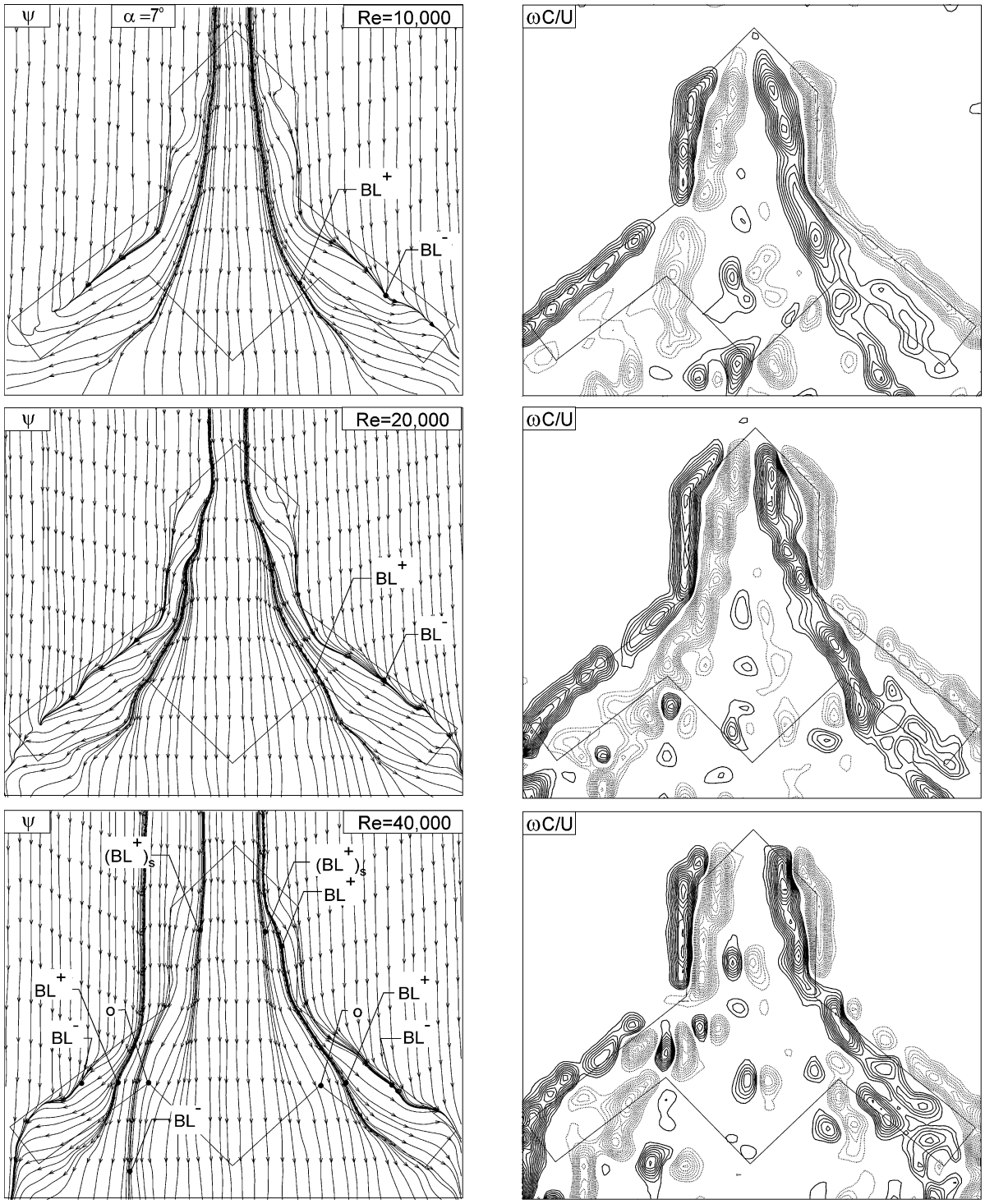

Fig. 6 Patterns of instantaneous streamline topology Ψ and normalized surface-normal vorticity $\omega C/U$.

center of the vortex emanating from the apex of the fuselage. At locations farther downstream, this shaded region exists below the dye markers that indicate the coexistence of the apex vortex and that arising from the wing junction. At higher values of $Re = 2 \times 10^4$ and 4×10^4, and at streamwise locations downstream of the wing junction, the shaded gray area of the vorticity contours moves in the outboard direction. Furthermore, at $Re = 4 \times 10^4$, it takes on a substantially distorted form. In fact, at this highest value of Reynolds number Re, two additional extrema of $\langle\omega\rangle C/U$ occur; they are designated l and m. This outboard migration of the shaded (highest) levels of vorticity is in accord with the outward deflection of the wing junction vortex evident in the dye visualization at $Re = 2 \times 10^4$ and 4×10^4 in Fig. 2a. A further interesting point is that the peak levels of vorticity $\langle\omega\rangle C/U$ designated by the shaded region do not change significantly with the location of onset of vortex breakdown. That is, as shown by the dye visualization in Fig. 2a, the onset of breakdown of the vortices emanating from the apex of the fuselage moves dramatically upstream with increasing Reynolds number Re. Yet, there seems to be no correlation between the magnitude of the surface normal vorticity $\langle\omega\rangle C/U$ associated with the swirling vortex flow above the wing and the occurrence or nonoccurrence of breakdown.

Patterns of Reynolds stress correlation $\langle u'v' \rangle / U^2$ are given in Fig. 5b. Minimum and incremental absolute values of Reynolds stress correlation $\langle u'v' \rangle / U^2$ are 0.0005 and 0.0005. Immediately adjacent to the leading edge, near the apex, a correlation peak p occurs. It is apparently associated with the severe three-dimensional distortion and the associated instability arising on either side of the apex. At, and downstream of, the wing junction, extrema of $\langle u'v' \rangle / U^2$ appear; they are designated r and s. These extrema represent correlations of substantial amplitude and physically have their origin in the instability/breakdown of the vortices arising from the apex and the wing junction. Furthermore, in the wake downstream of the wing notch, an additional extremum t appears. It is apparently due to highly correlated fluctuations in the breakdown region in the wake. Additionally, near the plane of symmetry of the wing, pairs of positive and negative extrema of $\langle u'v' \rangle / U^2$ occur, apparently due to an instability of the three-dimensional separation in that region.

At a higher value of $Re = 2 \times 10^4$, an additional extremum of q arises. It is located immediately upstream of the onset of vortex breakdown. At $Re = 4 \times 10^4$, this extremum q is well within the region of vortex breakdown shown in the visualization of Fig. 2a. With regard to the extrema r and s that were present at $Re = 1 \times 10^4$, their positions are relatively unchanged at higher values of $Re = 2 \times 10^4$ and 4×10^4. The extrema r have values $\langle u'v' \rangle / U^2 = -0.0063$, -0.0111, and -0.0075 for values of Reynolds number $Re = 1 \times 10^4$, 2×10^4, and 4×10^4, whereas the values at s have values of -0.0044, -0.0105, and -0.0229 for the same three sequential Reynolds numbers. The extrema s are located well downstream of the wing junction and, therefore, indicate the consequence of interaction between the junction and apex vortices, or lack of it, as well the onset of vortex breakdown. As shown in Fig. 2a, at $Re = 1 \times 10^4$, the vortices originating from the apex and the junction exhibit spiral forms as they intertwine. At the other extreme, for $Re = 4 \times 10^4$, no such interaction occurs. Rather, the apex vortex is in a broken down/turbulent state, and the junction vortex is deflected in the outboard direction. This latter pattern is associated with values of $\langle u'v' \rangle / U^2$ approximately five times larger than those arising from the former pattern, in accord with the foregoing extrema at s.

Furthermore, extrema t and w are evident in the region immediately downstream of the trailing edge of the wing. At $Re = 2 \times 10^4$, the extremum t has moved closer to the notch in the trailing edge and, in addition, additional extrema w are present. At $Re = 4 \times 10^4$, the pattern of t and w clusters has a broadly similar form to those at $Re = 2 \times 10^4$. The higher levels of Reynolds stress seen at $Re = 2 \times 10^4$ and $Re = 4 \times 10^4$ are associated with the different characteristics of vortex breakdown and vortex–vortex interaction, relative to those at $Re = 1 \times 10^4$. In addition, it may be influenced by enhanced transition of the shear layer separating from the leading edge of the planform, which may be felt on its surface. At the wing root, the separation process leading to formation of the root vortex is particularly complex, and may show an enhanced level of unsteadiness at higher values of Reynolds number.

Instantaneous Patterns of Near-Surface Streamline Topology and Surface-Normal Vorticity

Whereas Figs. 2–5 correspond to time-averaged patterns of the flow structure, instantaneous streamline $\langle \Psi \rangle$ and vorticity ω patterns

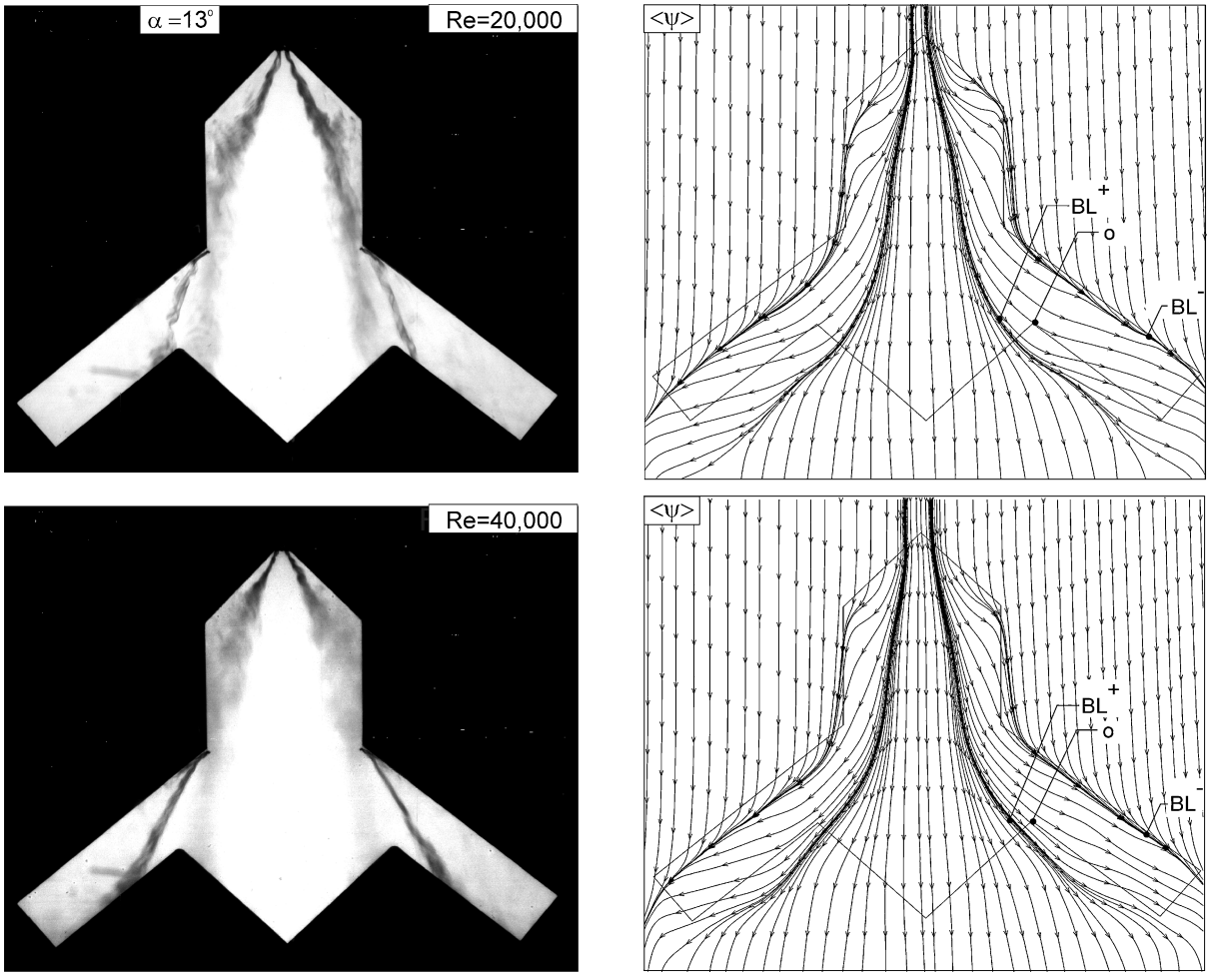

a) b)

Fig. 7 Comparison of patterns of dye visualization with near-surface patterns of streamline topology $\langle \Psi \rangle$, moderate angle of attack $\alpha = 13$ deg over range $Re = 2 \times 10^4$–4×10^4.

are shown for comparison in Fig. 6. For patterns of instantaneous dimensionless vorticity $\omega C/U$, minimum and incremental values are 2.0 and 1.0. Loci of positive and negative bifurcation lines are designated as BL^+ and BL^-. Such lines are clearly identifiable and, generally speaking, occupy the same positions on the planform as their time-averaged counterparts $\langle\Psi\rangle$ indicated in Fig. 2b. That is, the major topological features of the instantaneous Ψ are essentially the same as those for the time averaged $\langle\Psi\rangle$. In other words, no instantaneous representations of foci, which represent apparent centers of spiral streamline patterns or saddle points, which indicate apparent intersections of streamlines, are evident in the instantaneous patterns. This observation suggests that large-amplitude, time-dependent excursions of the onset of breakdown and surface separation do not occur.

Regarding the patterns of instantaneous dimensionless vorticity $\omega C/U$, shown in Fig. 6b, smaller-scale concentrations of vorticity are generally more evident than in the corresponding time-averaged pattern $\langle\omega\rangle$ given in Fig. 5a. In an overall sense, however, the positions of the highest levels of vorticity along the surface of the planform are in accord with those of the time-averaged patterns $\langle\omega\rangle$ given in Fig. 5a.

IV. Near-Surface Patterns at Moderate Angle of Attack

To clarify the effect of angle of attack α on the sensitivity to Reynolds number, images were acquired at $\alpha = 13$ deg. In the following paragraphs the central features of these patterns will be shown and then discussed in relation to those at lower angle of attack $\alpha = 7$ deg, which are described in the preceding section.

Patterns of Dye Visualization and Near-Surface Time-Averaged Streamline Topology

Dye visualization of the vortices emanating from the apex and the wing junction are given in Fig. 7a. Figure 7a were selected from the large number of visualizations of Elkhoury and Rockwell.[10] For all values of Reynolds number, the onset of vortex breakdown occurs relatively close to the apex of the fuselage. Although it has a somewhat different form for different Reynolds numbers, it is evident that an increase in Reynolds number does not result in a substantial change of the onset of vortex breakdown, as measured from the tip of the apex. For this reason, one expects a small degree of sensitivity to Reynolds number, in comparison with the dye visualization of Fig. 2a, which showed large changes in the onset of vortex breakdown with increase in Reynolds number.

On the other hand, it is evident that the angle of inclination of the vortex arising from the wing junction changes discernibly with increasing Reynolds number. That is, the centerline of this vortex is deflected in the outboard direction as Reynolds number increases. Patterns of averaged streamlines $\langle\Psi\rangle$, shown in Fig. 7b, have a generally similar form for values of $Re = 2 \times 10^4$ and 4×10^4. First consider the positive bifurcation line, designated as BL^+, and its position relative to the notch, designated as ○. Small changes occur with increasing Reynolds number, but the location of BL^+ is always inboard of the notch ○. Comparison of the distance between positive bifurcation lines BL^+ on either side of the wing indicate that as Reynolds number increases, this gap distance increases as well. This can be seen by comparison of the gap distance between the BL^+ at a location immediately upstream of the

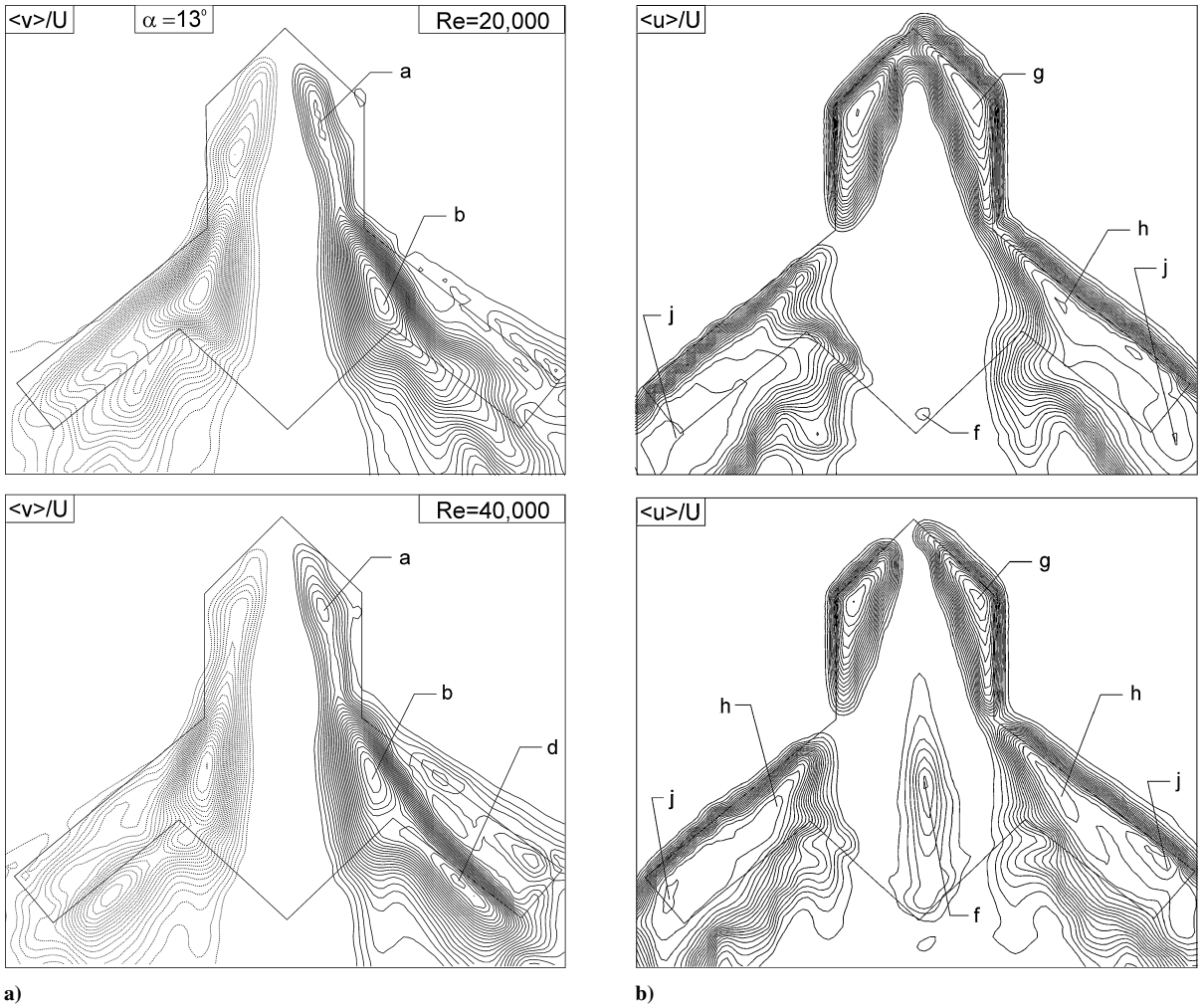

Fig. 8 Comparison of patterns of transverse $\langle v\rangle/U$ and streamwise $\langle u\rangle/U$ velocity contours, moderate angle of attack $\alpha = 13$ deg over $Re = 2 \times 10^4$–4×10^4: a) patterns of $\langle v\rangle/U$, extrema a, b, and d represent local maxima, and b) patterns of $\langle u\rangle/U$, extrema f through h and j represent local minima.

apex of the fuselage. With regard to the negative bifurcation lines BL^-, they show little change in position with increasing Reynolds number.

Patterns of Near-Surface Time-Averaged Transverse and Streamwise Velocity Components

Patterns of averaged transverse $\langle v\rangle/U$ and streamwise $\langle u\rangle/U$ velocity contours are given in Fig. 8. Minimum and incremental values of $\langle v\rangle/U$ are 0.05 and 0.025 and for $\langle u\rangle/U$ are 0.05 and 0.025. With regard to the contours of $\langle v\rangle/U$ given in Fig. 8a, it is possible to identify at $Re = 2 \times 10^4$ local maxima a and b, which have mirror images on the opposite side of the wing. With an increase to $Re = 4 \times 10^4$, the form and location of maxima a and b are nearly unaltered, although an additional maximum d appears at the trailing edge of the wing.

For the patterns of streamwise velocity component $\langle u\rangle/U$ given in Fig. 8b, it is possible to identify local minima, designated as g, h, and j at both $Re = 2 \times 10^4$ and 4×10^4, and at the higher Reynolds number of $Re = 4 \times 10^4$, the minimum j tends to move inboard of the wing tip. Furthermore, a distinctive feature of the patterns $\langle u\rangle/U$ of Fig. 8b is the cluster of contours along the plane of symmetry of the planform at $Re = 4 \times 10^4$; it has a minimum designated as f. The physical interpretation of this cluster is the same as for the similar clusters of Fig. 4b. Regions of flow deceleration and acceleration occur respectively upstream and downstream of the minimum f.

Taken together, the patterns of $\langle v\rangle/U$ and $\langle u\rangle/U$ given in Fig. 8 show a generally similar form at the two extreme values of Reynolds number $Re = 2 \times 10^4$ and 4×10^4, save for the region at the plane of symmetry. This relative invariance with increase in Reynolds number is in contrast to that occurring at relatively low angle of attack, as indicated in Fig. 4. Therein, it is evident that an increase to $Re = 4 \times 10^4$ is associated with an increase in the number of local peaks, that is, minima and maxima, of both $\langle v\rangle/U$ and $\langle u\rangle/U$. Therefore, we again conclude, as was the case for the corresponding near-surface streamline topology shown in Fig. 7b, that the patterns of $\langle v\rangle/U$ and $\langle u\rangle/U$ of Fig. 8 are relatively insensitive to Reynolds number.

Surface-Normal Vorticity and Near-Surface Reynolds Stress Correlations

Patterns of dimensionless surface-normal vorticity $\langle\omega\rangle C/U$ and Reynolds stress correlation $\langle u'v'\rangle/U^2$ are given in Fig. 9. For vorticity contours, minimum and incremental absolute value of $\langle\omega\rangle C/U$ are 1.0 and 1.0. Minimum and incremental absolute values of Reynolds stress correlation $\langle u'v'\rangle/U^2$ are 0.001 and 0.0005. Consider first the patterns of $\langle\omega\rangle C/U$, at the two extreme values of $Re = 2 \times 10^4$ and 4×10^4. They show relatively small differences, that is, the shaded region of positive vorticity along the starboard side of the wing has a remarkably similar form at both values of Reynolds number, except for the downstream tail of this shaded region, which follows the trailing edge of the wing extension more closely at the higher value of $Re = 4 \times 10^4$. Again, this contrasts with the case at $Re = 4 \times 10^4$ at the relatively low angle of attack in Fig. 5a, where the onset of well-defined clusters of vorticity, in conjunction with severe deflection and distortion of the shaded region of positive vorticity in the outward direction, is a major feature. Near the plane of symmetry of the wing, however, it is possible to detect well-defined clusters of out-of-plane vorticity designated as k

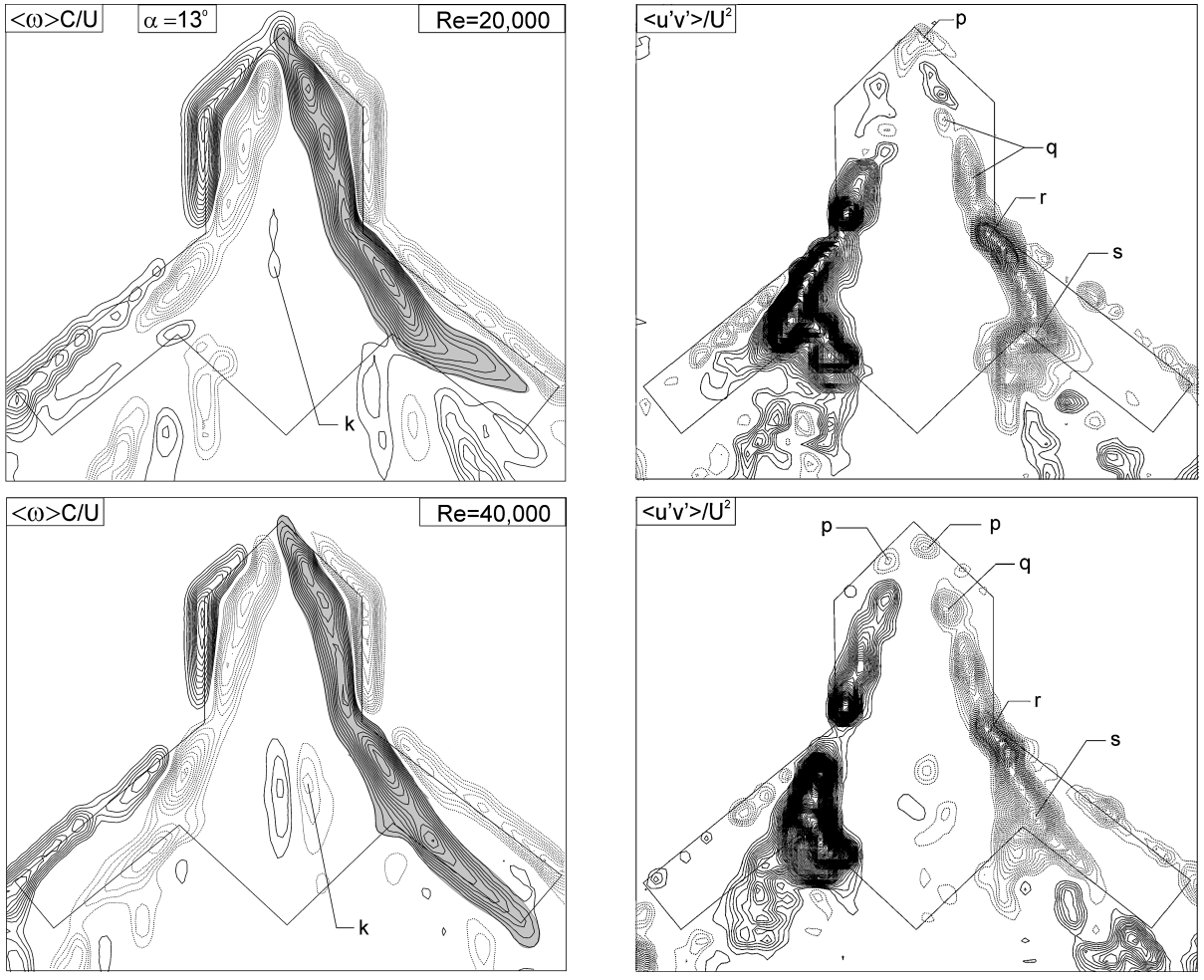

a) b)

Fig. 9 Comparison of patterns at moderate angle of attack $\alpha = 13$ deg over $Re = 2 \times 10^4$–4×10^4: a) normalized, time-averaged vorticity $\langle\omega\rangle C/U$ and b) Reynolds stress correlation $\langle u'v'\rangle/U^2$.

at the higher value of $Re = 4 \times 10^4$. This feature, along with clusters of vorticity in the wake region of the wing at $Re = 2 \times 10^4$, appear to be the predominant distinguishing features at the extreme values of Reynolds number. The surface-normal vorticity appears to indicate the presence of vortex(ices) above the surface of the planform, but as is evident by comparing the vorticity patterns of Fig. 9a for $\alpha = 13$ deg at $Re = 2 \times 10^4$ with the corresponding dye visualization of Fig. 7a, it is not always possible to identify each vortex in a dual vortex system.

The patterns of Reynolds stress correlation $\langle u'v' \rangle / U^2$, shown in Fig. 9b, indicate regions of relatively high level, which have substantial spatial extent in the region downstream of the wing junction. Furthermore, relatively high levels of $\langle u'v' \rangle / U^2$ are evident in the region upstream of the junction. They are designated as q, and at the larger Reynolds $Re = 4 \times 10^4$, they show higher levels closer to the apex of the fuselage. This observation is in accord with that of the dye patterns of Fig. 7a and is associated with the vortex breakdown that occurs closer to the apex of the fuselage at the higher value of Reynolds number. Nevertheless, it is remarkable that this discernible alteration of the onset of vortex breakdown seems to have little influence on the patterns of $\langle u \rangle / U$ and $\langle v \rangle / U$ in the region of the planform upstream of the junction at both values of Reynolds number. A generally similar observation holds for corresponding patterns of surface-normal vorticity $\langle \omega \rangle C / U$ in Fig. 9a.

V. Conclusions

The effects of Reynolds number on the near-surface patterns of a classical UCAV planform can be quantitatively interpreted in terms of streamline topology, especially bifurcation lines, as well as contours of streamwise and transverse velocity components, surface-normal vorticity, and Reynolds stress correlation. Taken together, these criteria provide complementary, explicit definitions that, when considered with qualitative dye visualization, provide a physically meaningful portrayal of the mechanisms associated with Reynolds number dependence.

At relatively low angle of attack, the core of the vortex is located relatively close to the surface of the planform and presumably interacts with the surface boundary layer. It is known from previous dye visualization that, with increasing Reynolds number, 1) the onset of vortex breakdown moves upstream a substantial distance, 2) decreased interaction occurs between the vortices formed from the apex and junction of the planform, and 3) the core of the junction vortex is deflected in the outboard direction. It is demonstrated herein that these features are associated with following quantitative trends.

1) Well-defined bifurcation lines, which are a basic class of topological pattern, exist immediately adjacent to the surface of the wing. With increasing Reynolds number, both positive and negative bifurcation lines are deflected in the outboard direction. Remarkably, the existence of these bifurcation lines and their outboard deflection are also clearly evident in the patterns of instantaneous streamlines, which means that they are a robust feature of the flow structure for all time and not a consequence of time-averaging distinctly different states of the flow.

These near-surface patterns are linked to corresponding crossflow patterns. At the low sweep angle of interest herein, reattachment of the shear layer to the wing surface, evident from patterns of velocity in the crossflow plane, is associated with the location of a positive bifurcation line, that is, attachment line, of the near-surface topology. As Reynolds number increases, this reattachment location moves in the outboard direction toward the leading edge, corresponding to an outboard displacement of the negative bifurcation line.

2) Patterns of surface-normal vorticity, which show large values beneath the cores of the dye-visualized vortices, undergo a deflection in the outboard direction similar to the deflection of the aforementioned bifurcation lines. Moreover, this deflection is also evident in the instantaneous images as well.

3) A local region of flow deceleration, followed by flow acceleration, occurs along the central portion of the planform. The location of the region of deceleration of the streamwise velocity along the plane of symmetry of the planform depends significantly on the value of Reynolds number.

4) Near the wing tips, regions of localized reverse flow are distinguishable at lower values of Reynolds number. They are eradicated, however, at higher values of Reynolds number.

5) In the region immediately downstream of the wing junction, where both the junction and apex vortices are present, large variations of the streamwise and transverse velocity components occur along the surface of the planform. A number of peaks are present in the contour patterns of these velocity components. They are, in turn, associated with the onset of well-defined clusters of surface-normal vorticity. Indications of these clusters are also identifiable in the pattern of instantaneous vorticity.

6) The foregoing time-mean features of the near-surface patterns are associated with regions of large Reynolds stress correlation at, and downstream of, the wing junction. Peak values of this dimensionless correlation are larger at higher values of Reynolds number, in accord with alterations of the onset of vortex breakdown and vortex–vortex interactions visualized by dye injection. Furthermore, regions of significant Reynolds stress correlation occur closer to the wing apex with increasing Reynolds number.

At moderate, rather than low, angle of attack, qualitative visualization of the core of the vortex emanating from the apex shows that it is displaced a significant elevation above the surface of the wing. Furthermore, the onset of vortex breakdown occurs relatively close to the apex over the range of Reynolds number examined. Because these effects, the changes in the near-surface topology and flow structure are generally much less sensitive to Reynolds number. The shift of the bifurcation lines and the patterns of surface-normal vorticity in the outboard direction, which was a prevalent feature at low angle of attack, is not evident. Furthermore, in the region of the planform downstream of the wing junction, the onset of multiple peaks in the patterns of the streamwise velocity component, as well as in the corresponding pattern of surface normal vorticity, does not occur at moderate angle of attack, in contrast to low angle of attack, where it was a central feature. With regard to the flow unsteadiness downstream of the wing junction, however, large magnitudes of Reynolds stress correlation occur in this region, as was the case at low angle of attack. As the Reynolds number is increased, the overall form of these patterns changes somewhat, and significant levels of the Reynolds stress correlation occur farther upstream, as observed at low angle of attack.

Acknowledgments

The authors are pleased to acknowledge support of the Air Force of Scientific Research, Grant F49620-02-1-0061, monitored by John Schmisseur.

References

[1]Hebbar, S. K., Platzer, M. F., and Fritzelas, A. E., "Reynolds Number Effects on the Vortical-Flow Structure Generated by a Double-Delta Wing," *Experiments in Fluids*, Vol. 28, No. 3, 2000, pp. 206–216.

[2]Verhaagen, N. G., "Effects of Reynolds Number on Flow over 76/40-Degree Double-Delta Wings," *Journal of Aircraft*, Vol. 39, No. 6, 2002, pp. 1045–1052.

[3]Visser, K. D., and Washburn, A. E., "Transition Behavior on Flat Plate Delta Wings," AIAA Paper 94-1850, June 1994.

[4]Verhaagen, N. G., Jenkins, L. N., Kern, S. B., and Washburn, A. E., "A Study of the Vortex Flow over a 76/40-deg Double-Delta Wing," AIAA Paper 95-0650, Jan. 1995.

[5]Yaniktepe, B., and Rockwell, D., "Flow Structure on a Delta Wing of Low Sweep Angle," *AIAA Journal*, Vol. 42, No. 3, 2004, pp. 513–523.

[6]Gordnier, R. E., and Visbal, M. R., "Higher-Order Compact Difference Scheme Applied to the Simulation of a Low Sweep Delta Wing Flow," AIAA Paper 2003-0620, Jan. 2003.

[7]Ol, M. V., and Gharib, M., "The Passage Towards Stall of Nonslender Delta Wings at Low Reynolds Number," AIAA Paper 2001-2843, June 2001.

[8]Ol, M. V., and Gharib, M., "Leading-Edge Vortex Structure of Nonslender Delta Wings at Low Reynolds Number," *AIAA Journal*, Vol. 41, No. 1, 2003, pp. 16–26.

[9]Yavuz, M. M., Elkhoury, M., and Rockwell, D., "Near-Surface Topology and Flow Structure on a Delta Wing," *AIAA Journal*, Vol. 42, No. 2, 2004, pp. 332–340.

[10]Elkhoury, M., and Rockwell, D., "Visualized Vortices on UCAV Planform: Effect of Reynolds Number," *Journal of Aircraft*, Vol. 41, No. 5, 2004, pp. 1244–1247.

[11]Taylor, G. S., Schnorbus, T., and Gursul, I., "An Investigation of Vortex Flows over Low Sweep Delta Wings," AIAA Paper 2003-4021, June 2003.

[12]Gursul, I., Taylor, G., and Wooding, C., "Vortex Flows over Fixed-Wing Micro Air Vehicles," AIAA Paper 2002-0698, Jan. 2002.

[13]Gursul, I., "Vortex Flows on UAVs: Issues and Challenges," *42nd Aerospace Sciences Meeting and Exhibit*; also AIAA Paper 2004-0892, Jan. 2004.

[14]Perry, A. E., and Fairly, B., "Critical Points in Flow Patterns," *Advanced Geophysics*, Vol. B14, 1974, pp. 299–315.

[15]Tobak, M., and Peake, D. J., "Topology of Three-Dimensional Separated Flows," *Annual Review of Fluid Mechanics*, Vol. 14, 1982, pp. 61–85.

[16]Lighthill, M. J., *Laminar Boundary Layers*, edited by L. Rosenhead II, Clarendon, Oxford, 1963, pp. 62–82.

[17]Squire, L. C., "The Motion of a Thin Oil Sheet Under the Boundary Layer on a Body," *Journal of Fluid Mechanics*, Vol. 11, 1961, pp. 161–179.

[18]Hunt, J. C. R., Abell, C. J., Petreka, J. A., and Woo, H., "Kinematical Studies of the Flow Around Free or Surface-Mounted Obstacles; Applying Topology to FlowVisualization," *Journal of Fluid Mechanics*, Vol. 86, 1978, pp. 179–200.